Journal of Engg. Research Vol. 7 No. (2) June 2019 pp. 25-44

Modeling direct contact membrane distillation using experimental data

Emad Ali

Chemical Engineering Department, King Saud University, Riyadh, Saudi Arabia, 11421
amkamal@ksu.edu.sa

ABSTRACT

A pilot plant is comprised of direct contact membrane distillation module that is used for brackish water desalination. The generated experimental data is used to validate a conventional mathematical model that describe the heat and mass transfer operations in such units. The model governing equations are calibrated judicially without over parameterization to make the model predictions accurate over a wide range of feed flow rates and temperature. Specifically, the discrepancy between the feed sensible heat and heat flux must be correlated to the process parameters and incorporated in the heat balance equations. This correction leads to enhanced prediction of the outlet permeate and brine temperatures. An ad hoc tuning parameter is added to the mass flux equating to improve the accuracy of mass production estimation. However, it is found that using a one-dimension model that accounts for variation of the bulk temperature along the membrane length can enhance the mass production prediction significantly without the need for unnecessary tuning parameter.

Keywords: membrane distillation, water desalination, model calibration, one-dimension model, heat loss.

INTRODUCTION

Direct contact membrane distillation is considered as an excellent process for water desalination due to many attractive features (Alklaibi & Lior, 2005; Alkhudairi et al., 2012; Phattaranawik and Jiraratananon, 2001; Raut and Kulkarni, 2012). DCMD is not sensitive to feed salinity because its driving force for water purification is the thermal difference across the membrane. Since separation mechanism is based on water vaporization, DCMD can achieve full rejection of salt ions and other non-volatile species. Because water vaporization occurs due to vapor pressure difference across the membrane, which does not mandate high temperature, DCMD energy requirements are low and hence can be operated by low-grade heat sources. DCMD can provide potable water for isolated and/or remote areas because of its simple structure. In fact, it requires low infrastructure and operates without connection to the electricity grid.

Despite the appealing characteristics of MD, it is not yet commercialized as a large-scale technology for water desalination (Nakoa et al., 2014; Khayet, 2010; Lawal and Khalifa, 2014; Pangarkar, 2011). This limitation is attributed to high membrane cost, scaling and fouling and low recovery ratio. Moreover, low recovery ratio leads to high specific energy consumption. For this reason, extensive research efforts are reported in the literature to deal with several aspects of MD design and operation. Several authors performed experimental and theoretical studies of brackish and seawater desalination using MD technologies (Nakoa et al., 2014; Lawal and Khalifa, 2014; Winter et al., 2011; Andrjesdóttir et al., 2013; Close and Sorensen, 2010). Other researchers sought performance improvement by incorporating process arrangements and/or configurations such as implementing heat recovery systems (Drioli et al., 205; Guan et al., 2015), employing brine recycling (Duong et al., 2015; Lokari et al., 2018) and the use of multi-stage concept (Drioli et al., 2015, Geng et al., 2015). Many researchers investigated the use of low-cost energy to operate the MD process. Appropriate integration of MD units with renewable energy sources can be found in Banat et al., 2007; Lienhard et al., 2012; Chen et al., 2010. Similarly, altering or modification of the membrane module structure such as the use of air-gap, vacuum, and sweeping gas and recently the development of water gap and material gap MD

(Khalifa, 2015; Francis et al., 2013; Swaminathan; 2016; Safavi & Mohammadi, 2009) are also studied. These cited references are just a sample of many others; in addition, several other efforts cannot be classified under the above categories. Nevertheless, this is an indication of growing work to enhance the MD efficiency and operation to reach the level of industrial application as a feasible water desalination technology.

In fact, DCMD performance in terms of water recovery is governed by coupled mass and heat transfer phenomena. Andrjesdóttir et al. (2013) indicated that despite the extensive experimental investigation, a better understanding of the heat and mass transport phenomena needs to be established. To the best of our knowledge, the use of experimental data to calibrate both the mass and heat transfer over a wide range of feed flow rate and temperatures is not widely investigated. This work is a continuation of an earlier study (Ali & Orfi, 2018). In earlier work, the conventional model of MD was able to match the experimental data for the various operating conditions without modification of the model physical parameters such as porosity, membrane coefficient, and heat transfer. This modification leads to over-parameterization of the process parameters for each feed flow rate and temperature. In this paper, we lay out a straightforward and judicious way to calibrate the theoretical model without resorting to offhand corrections or parameterizing the process physical parameters. In fact, a correction term will be added to the heat balance equation to account for model-plant mismatch arising from modeling error and/or heat losses. In addition, one-dimension model that address the temperature distribution with the length of the membrane sheet will be utilized. In fact, the one-dimension and two-dimension models for MD process have been investigated by others (Eleiwi et al., 2016; Chen et al., 2009; Zhang, 2011; Ashoor et al., 2012). Building a reliable model can facilitate the design and optimization of such important separation technology. In addition, the analysis associated with modeling procedure can supplement the perception of the fundamentals of the process and highlight the shortcomings of existing mathematical models

EXPERIMENTAL SETUP

The experimental data used here to validate the model is obtained from running a full-scale pilot-plant DCMD unit developed by Solar Spring. The MD module is characterized by a 10 m² effective membrane-area, 230 μm thickness of the membrane, 14 m channel-length, and 0.7 m channel-height, 0.2 μm pore diameter, and 2 mm channel-gap. A photo of the unit and the schematic of the process flow sheet are shown in Figures 1 and 2. Other details are given elsewhere (Ali & Orfi, 2018). The pilot plant provides data logging of various measurements including the water mass production, and the inlet and outlet temperatures of the hot and cold streams. The temperature of the inlet hot stream is regulated automatically using an external electrical heat exchanger. The temperature of the inlet cold permeate is maintained via a cooler using a chilled tap water as a coolant. The flow rate of the coolant is manipulated manually to control the temperature of the inlet permeate. A tap water with a salinity of 800 ppm is used a brackish water to be distilled. The inlet permeate temperature is maintained around 25 ^{o}C for all experiments.

Fig. 1 Solar Spring MD module.

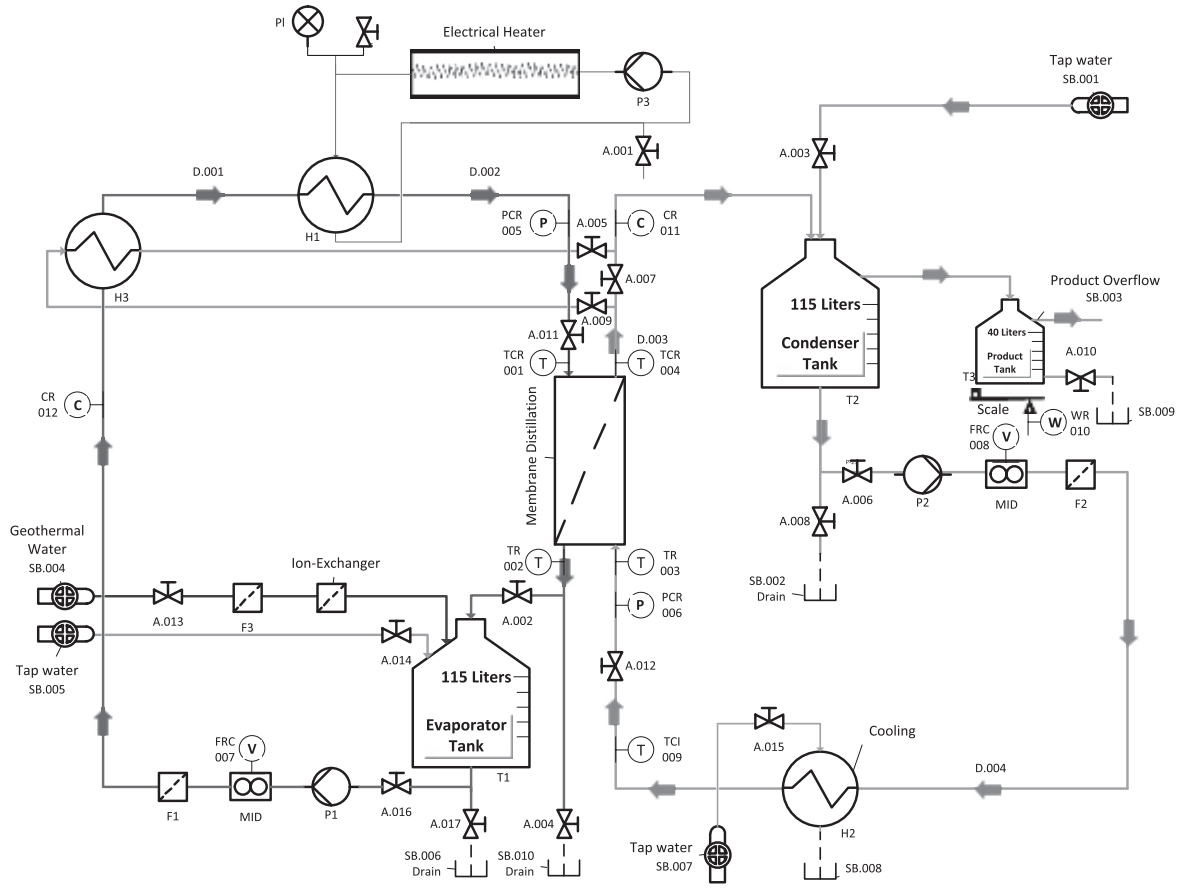

Fig. 2 Schematic of the experimental setup of the MD process flow sheet.

THE DCMD MODEL

The mathematical equations that describe the mass and heat transport phenomena in the membrane distillation are well developed in the literature (Nakoa, 2014; Mahmoudia, 2017). Description of the lumped-parameter model is given in earlier work (Ali & Orfi, 2018) and is summarized here.

The water vapor mass flux (J_w) traveling through the membrane pores can be calculated by

$$J_w = C_m(P_1 - P_2)\left(\frac{\frac{kg}{m^2}}{s}\right) \quad (1)$$

In Equation (1), P_1 and P_2 are the vapor pressures of water determined at the membrane interface temperatures T_{hm} and T_{cm}, respectively. Typical Antoine equation is used to estimate the vapor pressure (Khayet, 2010; Lawal and Khalifa, 2014):

$$P_1 = \exp(23.238 - \frac{3841}{T_{hm}-45})(1 - C_s)(1 - 0.5C_s - 10C_s^2) \quad (2)$$

$$P_2 = \exp(23.238 - \frac{3841}{T_{cm}-45}) \quad (3)$$

C_m is the membrane coefficient calculated from three correlations depending on the type of mass transfer regime:

Knudson flow mechanism:

$$C_m^k = \frac{2\varepsilon r}{3\tau\delta}\left(\frac{8M_w}{\pi RT}\right)^{1/2} \quad (4)$$

Molecular diffusion mechanism:

$$C_m^D = \frac{\varepsilon}{\tau\delta}\frac{PD}{P_a}\frac{M_w}{RT} \quad (5)$$

Knudsen-molecular diffusion transition mechanism:

$$C_m^C = \left[\frac{3}{2}\frac{\tau\delta}{\varepsilon r}\left(\frac{\pi RT}{8M_w}\right)^{1/2} + \frac{\tau\delta}{\varepsilon}\frac{P_a}{PD}\frac{RT}{M_w}\right]^{-1} \quad (6)$$

where T in Equations (4) to (6) is the average temperature at the membrane interface and given as follows:

$$T = \frac{T_{hm}+T_{cm}}{2} \quad (7)$$

The three flow regimes are based on the wall collision theory of water molecules. Each regime occurs at a specific range of values for the mean free path of a water molecule.

The heat transfer process occurs in three steps:

i. Convection from the feed bulk to the vapor-liquid interface at the membrane surface:

$$q_f = h_f(T_h - T_{hm}) \quad (8)$$

ii. Convection from the vapor-liquid interface at the membrane surface to the permeate side:

$$q_p = h_p(T_{cm} - T_c) \quad (9)$$

where h_f and h_p denote the heat transfer coefficients on the feed and cold stream sides, respectively.

iii. Evaporation and conduction through the microporous membrane:

$$q_m = J_w H_v + h_m(T_{hm} - T_{cm}) \quad (10)$$

where h_m is the conductive heat transfer coefficient and is equal to k_m/δ, where k_m and δ denote the membrane thermal conductivity and its thickness, respectively. H_v is the water latent heat, which can be estimated using Fard et al., 2015:

$$H_v(T) = 1850.7 + 2.8273\mathrm{T} - 1.6 \times 10^{-3}T^2 \quad (11)$$

The heat transfer coefficient in Equation (8) and (9) can be calculated using a correlation for the Nusselt number appropriate for laminar flow (Alkhudairi, 2012):

$$Nu = 0.298Re^{0.646}Pr^{0.316} \quad (12)$$

where Re is Reynolds number and Pr is Prandtl number.

The total heat flux across the membrane is directly proportional to the bulk temperature difference and can be expressed as follows:

$$H_t = U(T_h - T_c) \tag{13}$$

For countercurrent flow, the bulk temperatures are taken as $T_h = T_{h_{in}}$ and $T_c = T_{c_{out}}$.

The overall heat transfer coefficient is given by

$$U = \left[\frac{1}{h_f} + \frac{1}{h_m + \frac{j_w H_v}{T_{hm} - T_{cm}}} + \frac{1}{h_p}\right]^{-1} \tag{14}$$

Under steady-state operation, the heat transfer in the three individual parts of the system reaches equilibrium:

$$q_f = q_m = q_p \tag{15}$$

Considering the macroscopic scale of the MD unit (Figure 3), the heat balance around the permeate side is given by Zhang, 2011:

$$UA_s(T_h - T_c) = m_{c_{in}} \mathrm{c_p}\left(\mathrm{T_{c_{out}}} - \mathrm{T_{c_{in}}}\right) \tag{16}$$

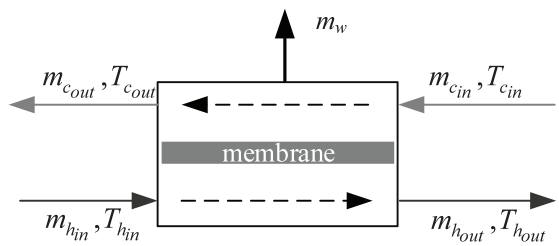

Fig. 3 Schematic of the membrane module

where m_c and C_p denote the mass flow rate and specific heat at a constant pressure, respectively. Equation (16) is used to compute the permeate exit temperature, $T_{c_{out}}$ Similarly, assuming a constant density and heat capacity, the mass and heat balance around the feed side is given by

$$UA_s(T_h - T_c) = m_{h_{in}} \mathrm{c_p}\left(\mathrm{T_{h_{out}}} - \mathrm{T_{in}}\right) \tag{17}$$

Equation (17) is used for computing $T_{h_{out}}$. Note we consider $m_{h_{in}} = m_{h_{out}}$ & $m_{c_{out}} = m_{c_{in}}$ because the mass production m_w is usually small compared to the feed mass rate. It should be noted in Equations (16) and (17) that the heat losses are ignored. A general formulation should be

$$UA_s(T_h - T_c) + H_{loss} = m_{c_{in}} \mathrm{c_p}\left(\mathrm{T_{c_{out}}} - \mathrm{T_{c_{in}}}\right) \tag{18}$$

$$UA_s(T_h - T_c) + H_{loss} = m_{h_{in}} \mathrm{c_p}\left(\mathrm{T_{h_{out}}} - \mathrm{T_{in}}\right) \tag{19}$$

The overall mass balance is written as follows:

$$m_{h_{in}} = m_{h_{out}} + m_w \tag{20}$$

$$m_{c_{out}} = m_{c_{in}} + m_w \tag{21}$$

m_w is simply the mass flux multiplied by the effective surface area. The definitions of various variables, the numerical values of physical and design parameters in equations and additional supporting correlations are provided in various references (Chen et al., 2010; Safavi an Mohammadi, 2009).

One-dimension model

The governing equations of the one-dimension model are simply the same as those of the lumper-parameters except that they are applied to an infinitesimal section of the membrane length denoted as control volume. A typical control element of width Δx where mass and heat transport occur is depicted in Figure 4. The heat and mass balance equations (18~21) are reformulated as follows (Zhang et al., 2011):

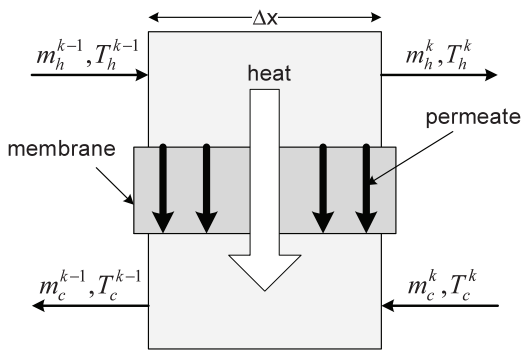

Fig. 4 mass and heat transport through a membrane control element.

$$U\Delta xh\left(T_h^k - T_c^k\right) + H_{loss} = m_c^k \mathrm{c_p}\left(\mathrm{T_c^{k-1}} - \mathrm{T_c^k}\right) \tag{22}$$

$$U\Delta xh\left(T_h^k - T_c^k\right) + H_{loss} = m_h^k \mathrm{c_p}\left(\mathrm{T_h^{k-1}} - \mathrm{T_h^k}\right) \tag{23}$$

$$m_h^k = m_h^{k-1} - m_w^k \tag{24}$$

$$m_c^k = m_c^{k-1} + m_w^k \tag{25}$$

These equations are solved sequentially starting from $x = 0$, corresponding to $k = 0$, which is the inlet point for the hot stream and finishes at $x = \mathrm{L}$, corresponding to $k = N$, which is the outlet point for the hot stream. L is the membrane length and h is the height. The rest of the equations and correlations for mass transfer, heat transfer, etc. used in the lumped-parameter model remain the same here**.** Note that the temperature gradient across the membrane width is neglected assuming the effect of the axial temperature distribution on mass and heat flux is more significant. Although the one-dimension and two-dimension models are applicable to flat sheet membrane, we implement them for spiral wound membrane for simplicity.

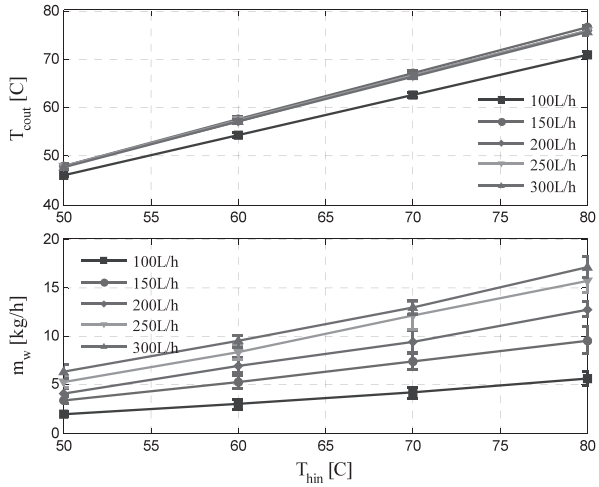

Fig. 5 Experimental measurement of and mass production at different feed flow rate and temperature.

RESULTS AND DISCUSSION

Experimental results

Figure 5 shows the pure experimental results owing to MD operation at different feed temperature and flow rate. Specifically, the figure shows two measured variables, namely, the water mass production, which is the main product of the unit and the permeate exit temperature. In fact, four stream temperatures are measured, but two of these temperatures are fixed such as the hot feed inlet temperature ($T_{h_{in}}$) and cold feed inlet temperature ($T_{c_{in}}$). Out of the remaining measured temperatures, the exiting permeate temperature is more crucial because it manifests the thermal effectiveness of the process in term of heat transfer from the hot side to the cooler side. The figure includes error bar to represent the standard of deviation resulting from several repetitions of the experiment. $T_{c_{out}}$ represents rational trend as it grows linearly with $T_{h_{in}}$ because the energy capacity grows with hotter feed. However, it depicts an interesting response to increasing feed flow rate. Indeed, $T_{c_{out}}$ response becomes almost identical with minor variation as feed flow rate exceeds 100 L/h. At high flow rates, the permeate temperature reaches a maximum value, which cannot be exceeded because of heat loss due to conduction and thermodynamic limitation, i.e., irreversibility. On the other hand, at flow rate of 100L/h and less, the heat losses to the soundings could be higher because of larger residence time enforced by low flow rate. The combination of increased heat loss to the surroundings and lower heat transfer coefficient due to lessened flow rate results in lower values for $T_{c_{out}}$. As far as the mass production is concerned, it illustrates compatible results to those reported in the literature especially in terms of its response to feed temperature and feed flow rate. For example, m_w grows with $T_{h_{in}}$ proportionally because of increasing thermal driving force leading to rapidly growing vapor pressure. Moreover, the mass production propagates with feed flow rate proportionally although the driving force, i.e., the temperature difference across the membrane (ΔT), saturates for flow rates higher than 100 L/h. Although (ΔT) saturates, a small variation still exists affecting water vaporization. In fact, mass flux depends not only on the temperature difference at the endpoints but also on the temperature difference along the membrane length. In fact, the bulk temperature may have different distributions along the length and thickness of the membrane as reported by (Eleiwi et al., 2016). An exception is at a flow rate equal to and less than 100 L/h where the mass production is lower even though it corresponds to higher driving force (ΔT). This can be attributed to reduced mass transfer coefficient due to reduced average membrane temperature. The behavior of $T_{c_{out}}$ and m_w will be further discussed using model simulation to seek better explanation of the process results.

Heat loss prediction

To make the MD model predict the process behavior over a range of feed temperature and flow rate as shown in Figure 5, the model must be calibrated. In Earlier work (Ali 7 Orfi, 2018) the model had to be overparametrized to match the measured data for each operating condition. To avoid such parameterization and maintain the model productiveness we seek judicious model modification. For this reason, we test the model using the measured data such as mass flux, j_w, exit permeate temperature, $T_{c_{out}}$, and hot feed temperature, $T_{h_{in}}$ as described by the phase 1 of the organigram shown in Figure 6. In this case, the measured data is used in the model to estimate the temperature at the membrane layers (T_{cm} & T_{hm}) and the overall heat transfer coefficient, U via iteration. At this phase, only the bulk temperature on each side is needed. For lumped-parameter model, the bulk temperature for the hot side is taken as $T_{h_{in}}$ and that for the cold side as $T_{c_{out}}$. Afterward, the sensible heat and heat transport are calculated where the measured $T_{c_{in}}$ and $T_{h_{out}}$ are also involved.

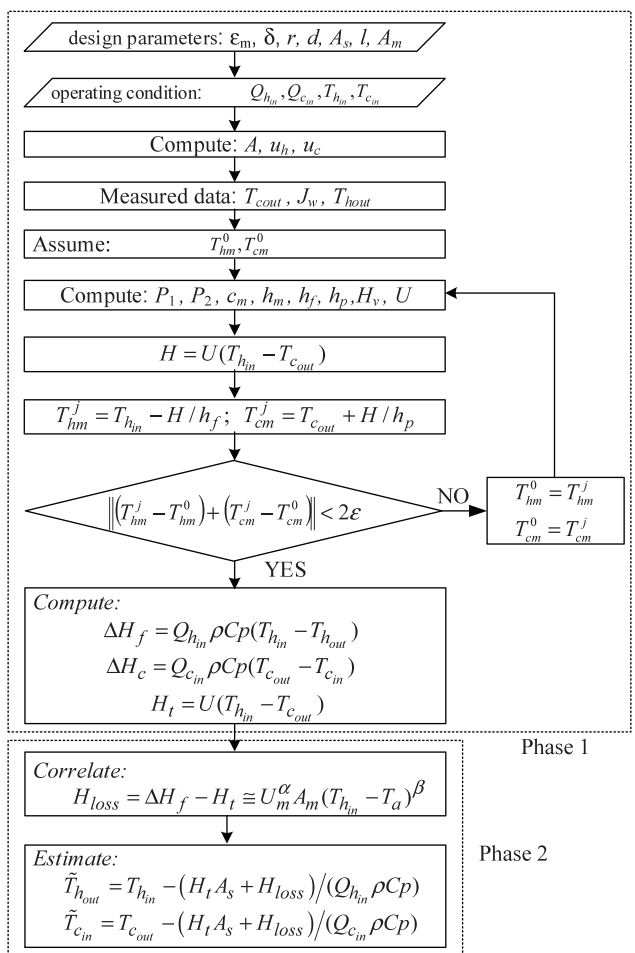

Fig. 6 Organigram for computing heat losses using measured data.

In phase 2 of the organigram, the inlet cold temperature $\tilde{T}_{c_{in}}$, and the outlet brine temperature $\tilde{T}_{h_{out}}$, are determined using heat balance on each side of the membrane which comprises sensible heat and heat loss correlation. Although $T_{c_{in}}$ is known a priori because it is fixed as an operating point, the solution algorithm for counter-current flow mandates assuming $T_{c_{out}}$ ahead to compute the inlet permeate temperature. The procedure is repeated until the calculated $\tilde{T}_{c_{in}}$ match the measured one. Calculation of the heat loss correlation is explained as follows.

Correction of Heat Balance

Figure 7 illustrates the sensible heat lost from the hot stream (ΔH_f), the sensible heat gained by the permeate stream (ΔH_c) and the heat transfer from the hot side to the cold side. As expected the sensible heat increases with both temperature and flow rate. The sensible heats for hot and cold streams are almost equal at high flow rate indicating minimum heat loss to the ambient. At low flow rate, i.e., 100L/h, a small discrepancy between ΔH_f and ΔH_c exists indicating possible heat loss to the ambient. At low flow rate, the heat transfer coefficient is trivial and the residence time of the fluid inside the membrane is high, which may lead to heat losses to the surroundings.

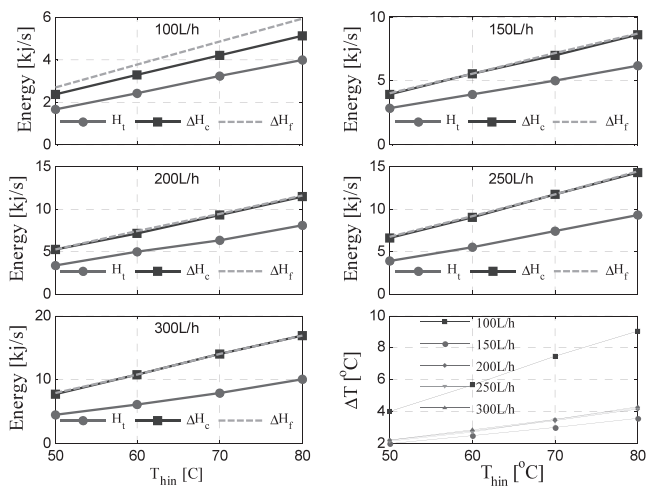

Fig. 7 Sensible heat and heat flux at different operating points.

Similarly, Figure 7 shows that the heat transport is proportional to feed flow rate and temperature because the heat transfer coefficient is likewise proportional to temperature and fluid velocity. The driving force ($\Delta T = T_{h_{in}} - T_{c_{out}}$), which is a major factor in the amount of heat transport, grows with feed temperature too as indicated in Figure 7. However, the feed flow rate has a different effect on the driving force. The latter has a large value at a flow rate equal to or less than 100L/h compared to those at higher flow rates. For high flow rates ranging from 150 L/h to 300 L/h, the driving force increases marginally with flow rate. The combined effect of heat transfer coefficient and ΔT creates the gap between the sensible heat and heat transferred. This indicates that the sensible heat extracted from the hot stream was not fully utilized as a portion of it is lost to the ambient, conduction resistance and/or thermodynamic irreversibility. Although uncertainty is associated with measured data, the sensible heat is considered reliable because it is based purely on measurement. In contrast, the amount of heat transferred is based on measurement and model correlations subject to modeling errors. Therefore, the gap between sensible heat and heat transferred can also be partially or fully due to modeling errors.

The heat loss to surroundings is minor and diminished with feed flow rate as discussed earlier. It can be neglected or added to Equation (19) to improve the prediction of $T_{h_{out}}$. The total heat loss is considerable and increases with feed flow rate as discussed earlier. The amount of energy loss must be incorporated in Equations (16 and 17) to improve the prediction of $T_{h_{out}}$ and $T_{c_{in}}$. Obviously, the total heat loss varies with feed temperature and flow rate as shown in Figure 7; hence it must be correlated to both temperature and flow rate to make Equations (18 and 19) predictive over a wide range of operation conditions. The easiest way is to formulate the heat loss as a common heat transfer law as follows:

$$H_{loss} = U_m^{\alpha} A_m \Delta T^{\beta} \tag{26}$$

where U_m and A_m are the overall pseudo-heat transfer coefficient and surface area for the module, respectively. In Equation (26), the temperature effect is involved explicitly, and the effect of flow rate is involved implicitly via U_m. Since this is an approximation and to cover a wide range of operating points, the correlation is tuned via the calibration parameters, i.e., α and β. The pseudo-heat transfer coefficient is calculated using Nusselt number for the average fluid inside the membrane. The pseudo temperature difference ΔT is taken as the difference between the hot fluid bulk temperature and the ambient temperature. The correlation is fitted to the measured heat loss by numerical optimization. The calibration parameters are found to be α = 2.33 and β = 0.66. Note that these parameters are fixed; i.e., they do not need retuning each time the model is used. In addition, these parameters are global, which means they can be used for the entire operating conditions shown in Figure 5. To test the effectiveness of the calibrated heat loss correlation, phase 2 of the organigram is conducted and the result is demonstrated in Figures 8 and 9. The estimated inlet permeate temperature and brine outlet temperature are in good agreement with the corresponding measured values; e.g., the differences are within 1 °C. The behavior of $T_{c_{in}}$ shows fuzziness and ambiguines because higher uncertainty is associated with its measured value. High and frequent fluctuation are observed in $T_{c_{in}}$ due to sensor uncertainty as well as the manual control of the coolant flow rate to regulate the permeate inlet temperature. Note that experimental data was used to estimate the heat losses and consequently $T_{c_{in}}$& $T_{h_{out}}$ to minimize the effect of modeling error. Moreover, the heat losses to the surrounding, $T_{c_{in}}$& $T_{h_{out}}$ have a distinguished trend at a flow rate of 150 L/h. A thorough thermodynamic analysis is carried out for this purpose and will be published shortly.

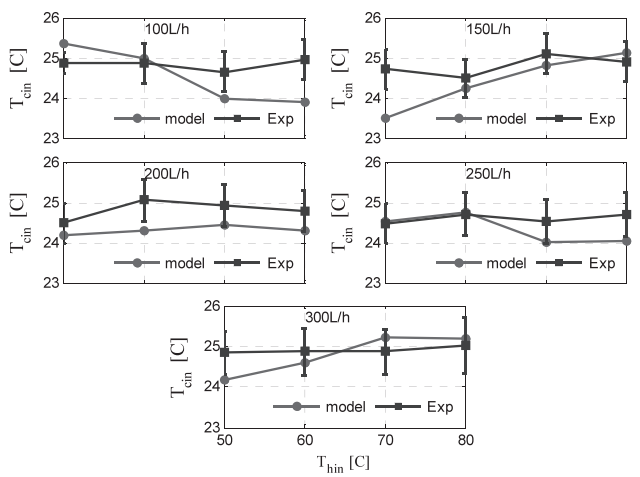

Fig. 8 Inlet permeate temperature profile using the model coupled with measured data.

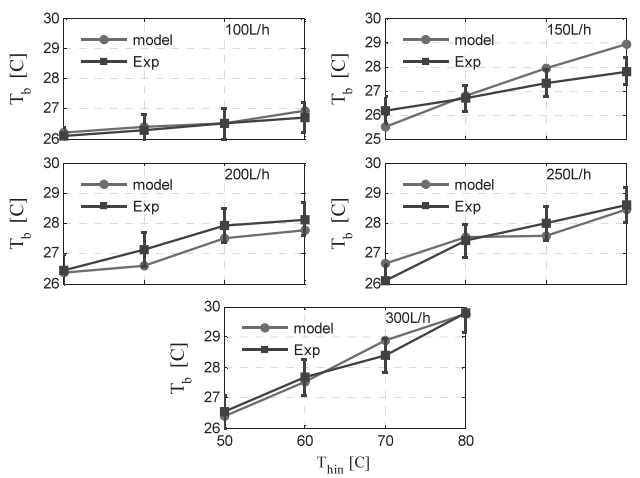

Fig. 8 Outlet Brine temperature profile using the model coupled with measured data.

Model prediction of mass flux

It is crucial to improve the model thermal prediction via adjusting the heat balance before seeking enhancement of model prediction of mass production. Although the heat balance part of the model is not directly involved in the mass transfer calculations, they are interrelated via the overall heat transfer coefficient, U. Moreover, $T_{c_{out}}$ has a direct influence on the mass production where, in counter-current flow pattern, accurate estimation of $T_{c_{out}}$ is necessary to ensure perfect prediction of mass flux. The model is simulated according to the organigram shown in Figure 10. In this case, the model is solved to determine the mass flux/production, permeate outlet temperature, and brine outlet temperature. No measured data is used except the input conditions, e.g., feed flow rate and feed temperatures for the cold and hot streams. The predicted mass production is shown in Figure 11. The dotted line indicates departure of the predicted mass flux away from the measured one. The problem with the model prediction of J_w is that the water vapor pressure grows exponentially with temperature which makes the model-based mass flux diverge away from the measured value especially at high temperatures. One way to reduce the rapid growth of the predicted J_w with temperature is to reduce the membrane mean temperature, i.e., to make T_{mh} closer to T_{cm}. However, since T_{hm} and T_{cm} cannot be measured, it is impossible to validate the computed membrane interface temperatures. Alternatively, we choose to use damping factor as follows:

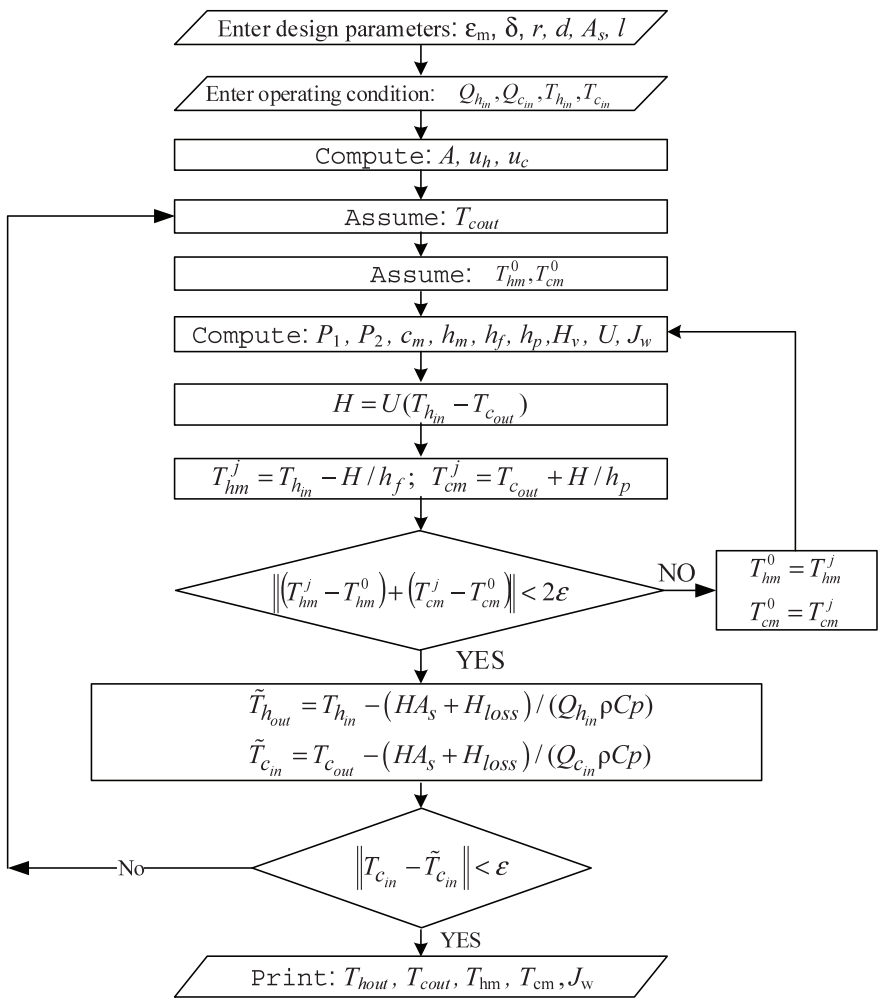

Fig. 10 Organigram for MD model solution.

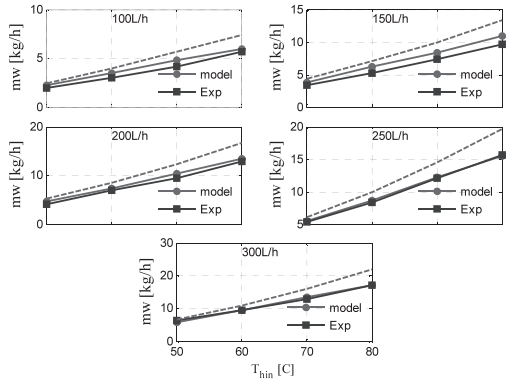

Fig. 11 MD mass production at selected feed flow rate and temperatures, $T_{c_{in}} = 25\,^{o}C$, dashed line: model without damping factor.

$$J_w = C_m(P_1 - P_2)^{0.8} \qquad (27)$$

Implementing the modified formula for the mass flux, the predicted mass production is enhanced substantially as shown in Figure 11. The corresponding predicted outlet temperatures are depicted in Figures 12 and 13. Note that $T_{c_{out}}$ is calculated here for given $T_{c_{in}}$ which shows perfect match of the experimental data except for flow rate of 100 L/h. $T_b = T_{h_{out}}$ delivered good match of the measured data except at low lowest flow rate. Note that the heat loss correlation (Equation (26)) is fitted using data for flow rates range of 150~300 L/h only. The inclusion of the data for a flow rate of 100 L/h will sacrifice the performance for all operating flow rates because the heat loss correlation has only two degrees of freedom, i.e., α & β.

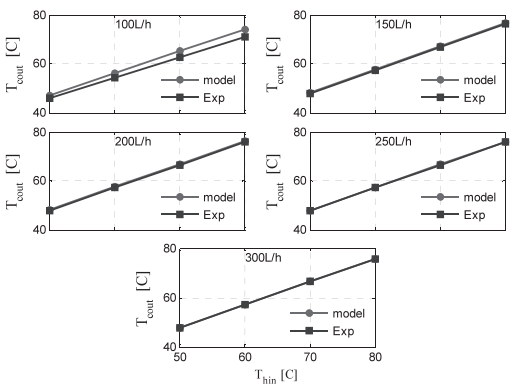

Fig. 12 model-predicted $T_{c_{out}}$ at selected feed flow rates and Temperature with $T_{c_{in}} = 25^{o}C$.

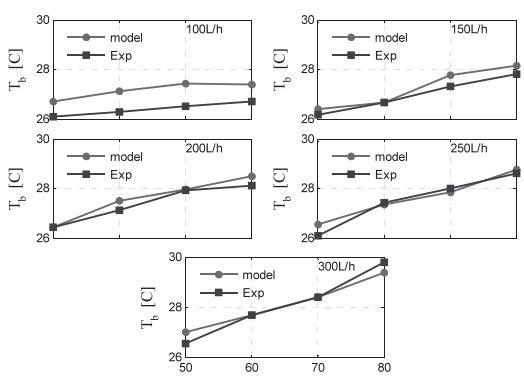

Fig. 13 model-predicted $T_b = T_{h_{out}}$ at selected feed flow rates and Temperature with $T_{c_{in}} = 25^{o}C$.

One-dimension MD model

Previous model results are based on a lumped-parameter model, which suffers from a notable mismatch between the predicted and measured mass flux when no damping factor is utilized. Another way to enhance the model prediction is to use one-dimension model to capture the complex relation between the mass and heat fluxes. By one-dimension, we mean the axial-direction *x* that represents the membrane longitude. In fact, as a long membrane sheet is utilized, it is essential to study the variation of the process variables with the x-axis, i.e., membrane length. The solution algorithm for solving the one-dimension model is depicted in Figure 14.

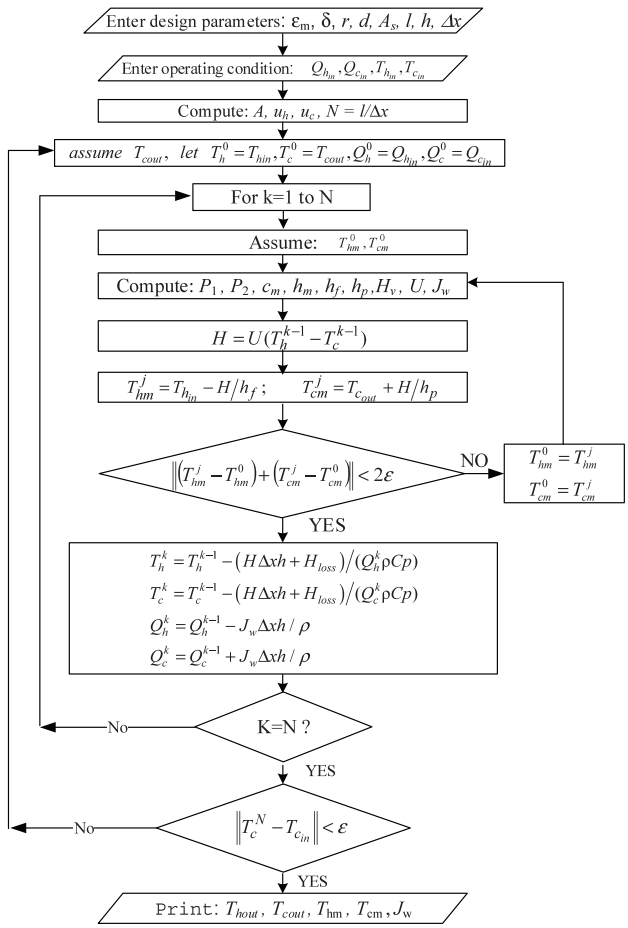

Fig. 14: Organigram for the solution of the one-dimension model.

In this algorithm, the MD model equations and correlations remain the same; however, the solution procedure is carried out on infinitesimal volume along the membrane length. The solution starts at the edge where the hot stream is fed, corresponding to $x = 0$, and finishes at the other edge where the hot stream exits, which corresponds to $x = L$. At $x = 0$, the temperature of the hot stream is prespecified; however, since we are dealing with counter-current flow regime, the temperature of the exiting permeate is unknown. Therefore, $T_{c_{out}}$ is assumed and the solution mechanism proceeds step-wise till the end of membrane length. The computed permeate temperature at $x = L$ must equal the prespecified permeate inlet temperature ($T_{c_{in}}$). If they match, the solution algorithm stops; otherwise, the procedure is repeated again. Within this iteration loop, another inner iteration is carried out to determine the membrane interface temperatures. Unlike the lumped-parameter model, the heat balance equations play a crucial role in calculating the mass transfer. In the lumped-parameter model, the heat balance equations specify the brine and permeate temperatures

at the terminal point of the MD module, which has no influence on the mass transfer calculations. In the one-dimension model, the computed brine and permeate temperatures are used as the feed temperatures for the next control volume, i.e., an infinitesimal section of the membrane length. These interim temperatures affect the calculated mass flux within the membrane section. This mechanism is repeated for the entire sections comprising the membrane length. The generated temperature and mass flux gradient are shown in Figure 15 for feed flow rate of 300 L/h. It is clear that both the bulk and membrane interface temperatures vary considerably with membrane length. The trend becomes narrower and slightly nonlinear at high hot feed temperatures. This behavior made the calculated mass flux vary substantially from the inlet to the outlet point membrane module. A similar simulation can be obtained for other flow rates. As a result, enhanced prediction of the mass production is obtained as illustrated in Figure 16. Note that the estimated mass flux in the one-dimension model does not utilize the $damping$ factor implemented in the lumped-parameter model. The other corresponding outputs of the model such as the exit permeate and brine temperatures are also demonstrated in Figures 17 and 18. The outlet permeates temperature presented perfect match of the measured data overall selected operating points because the model solution algorithm imposes constraints on $T_{c_{in}}$ which is strongly related to $T_{c_{out}}$. The outlet brine temperature delivered good agreement with the measured values with a maximum discrepancy of 1.2 ^{o}C. Better tracking of the plant data can be sought by imposing additional constraint in the solution algorithm but this will be at the expenses of adding additional tuning parameter or altering one of the process parameters. But we chose to keep the model as simple as possible.

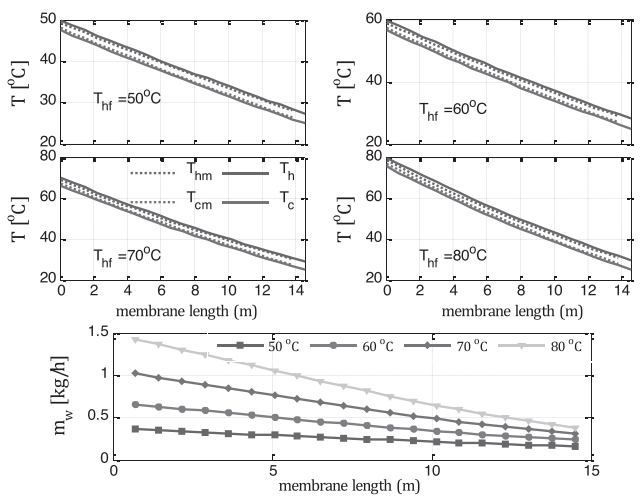

Fig. 15 Temperature and mass flux gradient along membrane length for Q = 300 L/h.

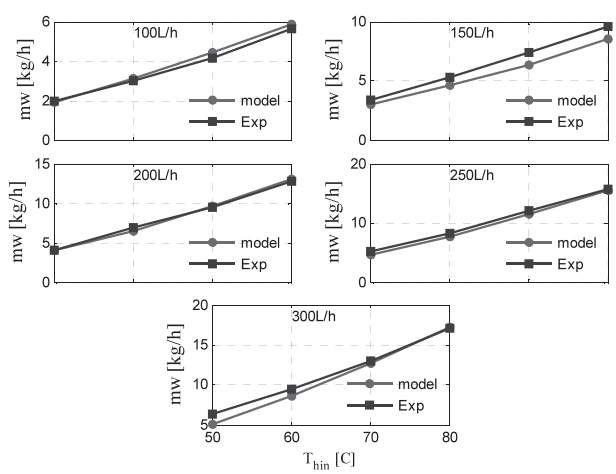

Fig. 16: Mass production profile obtained by using one-dimension model.

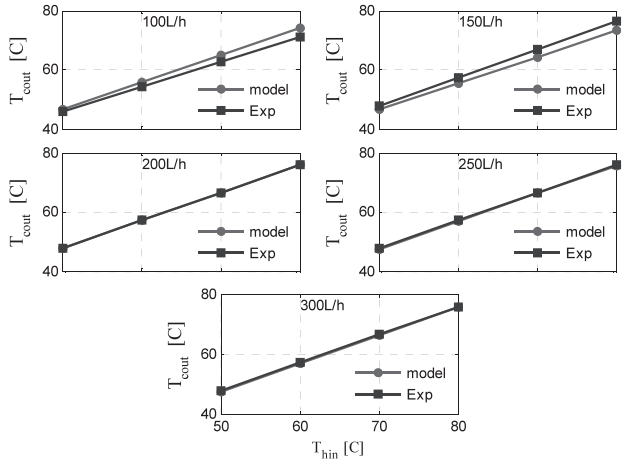

Fig. 17 Outlet permeate temperature for selected operating conditions using one-dimension model.

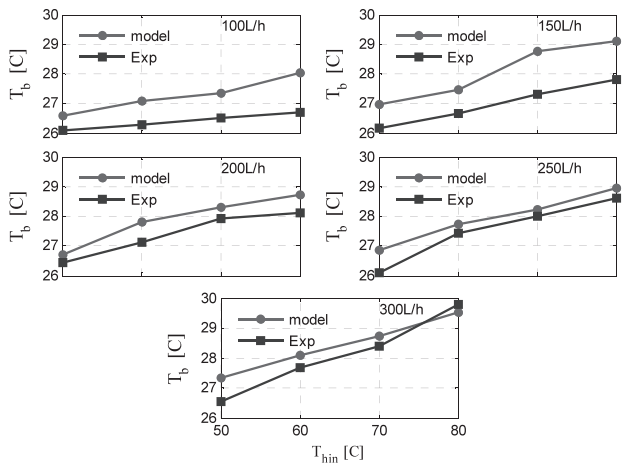

Fig. 18 Outlet brine temperature for selected operating conditions using one-dimension model.

CONCLUSIONS

Typical mathematical model for direct contact membrane distillation is fitted using experimental data over a range of operating conditions for the feed flow rate and temperature. The model equations calibration is achieved without over-parameterization of the process parameters to keep the value of the physical parameters of the process meaningful and reasonable. It is found that augmenting the heat balance equations by adequate heat loss estimation is crucial to improve the prediction of the thermal behavior of the process. However, the lumped-parameter model suffers from significant mismatch in predicting the mass flux/production. This is because lumped-parameter model considers the bulk temperature for the cold and hot sides constant over the entire length of the membrane sheet. For this purpose, a one-dimension model is utilized and provided excellent estimation of the mass production. The maximum and average calculated relative errors in the mass production are 19 and 6.6 %, respectively.

ACKNOWLEDGMENT

The project was supported by King Saud University, Deanship of Scientific Research, College of Engineering Research Center.

NOMENCLATURE

A_s	Surface area, m^2
A	Cross-sectional area, m^2
A_m	Hypothetical surface area, m^2
C_m	Permeability coefficient, kg/m^2sPa
C_m^k	Knudsen mass flux coefficient, kg/m^2sPa
C_m^d	Moléculaire diffusion mass flux coefficient, kg/m^2sPa
C_m^c	Transition mass flux coefficient, kg/m^2sPa
C_p	Heat capacity, J/kg K
C_s	Salt concentration, %
H_v	Latent heat of vaporization, J/kg
H_t	Overall heat flux, W/m^2
H_{loss}	Heat loss, kW
H_f	Feed sensible heat, kw
H_c	Permeates sensible heat, kw
h_f, h_p, h_m	Feed, permeate, and membrane heat transfer coefficient, W/m^2 K
h	Membrane channel height, m
J_w	Mass flux, kg/m^2 h
k_m	Membrane conductivity, W/m K
L	Membrane length, m
M_w	Molecular weight of water, g/mole
$m_{h_{in}}, m_{h_{out}}$	Hot water inlet and outlet flow rate, respectively kg/h
$m_{c_{in}}, m_{c_{out}}$	Cold water inlet and outlet flow rate, respectively kg/h
m_w	distillate flow rate, respectively, kg/h
Nu	Nusselt Number
N	Number of divisions of the membrane length
P_1, P_2	Vapor pressure at feed and permeate membrane surface, Pa
PD	Membrane pressure multiplied by diffusivity, Pam^2/s
P_a	Entrapped air pressure, Pa
Pr	Prandtl number
q_f, q_p	Heat transfer rate at feed and permeate sections, W/m^2
q_m	Heat of evaporation and conduction, W/m^2

r	Pore size, m
R	Ideal gas constant, J/mole K
Re	Reynold Number
T_h, T_c	Feed (hot) and permeate (cold) bulk temperature, K
T_{hm}, T_{cm}	Feed and permeate membrane temperature, K
$T_{h_{out}}, T_{h_{in}}$	Outlet and inlet hot feed temperature, C
$T_{c_{out}}, T_{c_{in}}$	Outlet and inlet cold stream temperature, C
U	Overall heat transfer coefficient, W/m^{2}K
U_m	Pseudo overall heat transfer coefficient, W/m^{2}K
x	x- axis

Greek letters

α	Heat loss tuning parameter
β	Heat loss tuning parameter
ε_m	Porosity
ε	Termination criteria
τ	Membrane tortuosity
δ	Membrane thickness, mm
ρ	Density, kg/m^3
Δ	Difference operator

REFERENCES

Ali, E. & Orfi, J. 2018. An experimentally calibrated model for heat and mass transfer in full-scale direct contact membrane distillation, Desalination and Water Treatment, **116**:1-18.

Alkhudhiri, A., Darwish, N. & Hilal, N. 2012. Membrane Distillation: A Comprehensive Review, Desalination, **287**:2-18, https://doi.org/10.1016/j.desal.2011.08.027

Alklaibi, A.M. & Lior, N. 2005. Membrane-distillation Desalination: Status and Potential, Desalination,**171**:111-131, https://doi.org/10.1016/j.desal.2004.03.024

Andrjesdóttir, O., Ong, C.L., Nabavi, M. Paredes, S., Khalil, A.S.G., Bruno, M. & Poulikakos, D. 2013. An Experimentally Optimized Model for Heat and Mass Transfer in Direct Contact Membrane Distillation, International Journal of Heat and Mass Transfer, **66**: 855–867. https://doi.org/10.1016/j.ijheatmasstransfer.2013.07.051

Ashoor, B., Fath, H., Marquardt, W. & Mhamdi, A. 2012. Dynamic modeling of direct contact membrane distillation processes, Computer Aided Chemical Engineering, **31**: 170-174, https://doi.org/10.1016/B978-0-444-59507-2.50026-3.

Banat, F., Jwaied, N., Rommel, M., Koschikowski, J. & Wieghaus, M. **2007.** Desalination by a "compact SMADES" autonomous solar-powered membrane distillation unit, Desalination, **217**:29–37. https://doi.org/10.1016/j.desal.2006.11.027

Chen, T-C, Ho, C-D & Yeh, H-M. 2009. Theoretical modeling and experimental analysis of direct contact membrane distillation,

Journal of Membrane Science **330**: 279–287, https://doi.org/10.1016/j.memsci.2008.12.063

Chen, T-C. & Ho, C-D. 2010. Immediate Assisted Solar Direct Contact Membrane Distillation in Saline Water Desalination, Journal of Membrane Science, **358**:122-130. https://doi.org/10.1016/j.memsci.2010.04.037

Close, E. & Sørensen, E. 2010. Modelling of Direct Contact Membrane Distillation for Desalination, 20th *European Symposium on Computer Aided Process Engineering* – ESCAPE20, Italy

Drioli, E., Ali, A. & Macedonio, F. 2015. Membrane Distillation: Recent Developments and Perspectives, Desalination, **356**: 56-84. https://doi.org/10.1016/j.desal.2014.10.028

Duong, H. C., Cooper, P., Nelemans, B., Tzahi, Y. C. & Nghiem, L.D. 2015. Optimising Thermal Efficiency of Direct Contact Membrane Distillation by Brine Recycling for Small-scale Seawater Desalination, Desalination, **374**: 1-9**.** https://doi.org/10.1016/j.desal.2015.07.009

Eleiwi, F., Ghaffour, N., Alsaadi, A.S., Francis, L. & Laleg-Kirati, T-M. 2016. Dynamic modeling and experimental validation for direct contact membrane distillation (DCMD) process, Desalination, 384, **15**: 1-11. https://doi.org/10.1016/j.desal.2016.01.004

Fard, K., Manawi, Y.M., Rhadfi, T., Mahmoud, K.A. Khraisheh, M. & Benyahia, F. 2015. Synoptic Analysis of Direct Contact Membrane Distillation Performance in Qatar: A Case Study, Desalination, **360**: 97–107. https://doi.org/10.1016/j.desal.2015.01.016

Francis, L., Ghaffour, N., Alsaadi, A.A. & Amy, G.L. 2013. Material gap membrane distillation: A new design for water vapor flux enhancement. J. Membrane Science, **448**: 240–247. https://doi.org/10.1016/j.memsci.2013.08.013

Geng, H., Wang, J., Zhang, C., Li, P. & Chang, H. 2015. High Water Recovery of RO Brine Using Multi-Stage Air Gap Membrane Distillation, Desalination, **355**: 178–185. https://doi.org/10.1016/j.desal.2014.10.038

Guan, G., Yang, X., Wang, R. & Fane, A.G. 2015. Evaluation of Heat Utilization In Membrane Distillation Desalination System Integrated With Heat Recovery, Desalination, **366**: 80-93. https://doi.org/10.1016/j.desal.2015.01.013

Khalifa, E. 2015. Water and air gap membrane distillation for water desalination—An experimental comparative study. Separation Purification Technology, **141**: 276–284. https://doi.org/10.1016/j.seppur.2014.12.007

Khayet, M. 2010. Desalination by Membrane Distillation. In: Encyclopedia of Life Support Science (EOLSS), Water and Wastewater Treatment Technologies.

Lawal, D.U. & Khalifa, A.E. 2014. Flux Prediction in Direct Contact Membrane Distillation, International Journal of Materials, International journal of Mechanics, Materials and Manufacturing, **2**(4):302-308. DOI: 10.7763/IJMMM.2014.V2.147

Lienhard, J.H., Antar, M.A., Smith, A., Blanco, J. & Zaragoza, G. 2012. Solar Desalination. Annual Reviews of Heat Transfer, 15, Article 4659. 10.1615/AnnualRevHeatTransfer.2012004659

Lokare, O.R., Tavakkoli, S. , Khanna, V. & Vidic, R.D. 2018. Importance of feed recirculation for the overall energy consumption in membrane distillation systems, Desalination, **428**: 250–254. https://doi.org/10.1016/j.desal.2017.11.037

Mahmoudia, G. M., Goodarzia, S.D. & Akbarzadeha, A. 2017. The Experimental and theoretical study of a lab scale permeate gap membrane distillation setup for desalination, Desalination, **419**: 197–210. https://doi.org/10.1016/j.desal.2017.06.01

Nakoa, K., Date, A. Akbarzadeh, A. 2014. A Research on Water Desalination Using Membr ane Distillation, Desalination and Water Treatment, 1- 13. https://doi.org/10.1080/19443994.2014.972731

Pangarkar, B.L., Sane, M.G. & Guddad, M. 2011. Reverse Osmosis and Membrane Distillation for Desalination of Groundwater: A Review, ISRN Materials Science, Volume 2011, Article ID 523124, 1-9. http://dx.doi.org/10.5402/2011/523124

Phattaranawik, J. & Jiraratananon, R. 2001. Direct Contact Membrane Distillation: Effect of Mass Transfer on Heat Transfer, Journal of Membrane Science, **188**:137-143. https://doi.org/10.1016/S0376-7388(01)00361-1

Raut R.P. & Kulkarni, K.S. 2012. Desalination by Membrane Distillation, International Journal of Advanced Engineering Research and Studies (open source), **1**(3) : 115-121.

Safavi, M. & Mohammadi, T. 2009. High-salinity Water Desalination Using VMD, Chemical Engineering Journal, **149**: 191-195. https://doi.org/10.1016/j.cej.2008.10.021

Swaminathan, J., Chung, H.W., Warsinger, D., Al-Marzooqi, F., Arafat, H.A. & Lienhard, J.H. 2016. Energy efficiency of

permeate gap and novel conductive gap membrane distillation. J Membrane Science, **502**: 171–178. https://doi.org/10.1016/j.memsci.2015.12.017

Winter, D., Koschikowski, J. & Wieghaus, M. 2011. Desalination Using Membrane Distillation: Experimental Studies on Full Scale Spiral Wound Modules, Journal of Membrane Science, **375**:104–112. https://doi.org/10.1016/j.memsci.2011.03.030

Zhang, J. 2011. Theoretical and Experimental Investigation of Membrane Distillation, Ph.D. Thesis, Victoria University, Australia.

Submitted: 21/06/2018
Revised: 10/03/2019
Accepted: 14/03/2019

نمذجة التقطير الغشائي المباشر باستخدام البيانات التجريبية

عماد علي
قسم الهندسة الكيميائية جامعة الملك سعود، الرياض، المملكة العربية السعودية

الخلاصة

تم استخدام وحدة معملية لتحلية المياة المالحه بالتقطير الغشائي لهذه الدراسة، حيث استخدمت البيانات المعملية لتوثيق نموذج رياضي تقليدي يصف عمليات انتقال المادة و الحراره داخل الأغشية. تم من خلالها معايرة النموذج الرياضي بحكمة بدون تعقيدات اضافية للمحافظه على قدرة النموذج للتنبؤ على نطاق واسع من ظروف التشغيل لدرجات الحرارة ومعدل تدفق المدخلات. على وجه التحديد تم ربط الفروقات بين الحرارة الكامنه والحرارة المنتقلة بمعاملات النموذج الرياضي واضافتها إلى معادلة التوازن الحراري. أدى هذا التحسين إلى رفع كفاءة النموذج الرياضي للتنبؤ بدرجات حرارة السوائل الناتجه مثل المياه المحلاه النافذة والمملحه. كما تم إضافة معامل ضبط في معادلة تدفق الكتله النافذه لتحسين حساب معدل كتلة المياه المحلاه. كما تم تطوير نموذج رياضي للوحده بحيث يشمل تغير درجات الحرارة المجمله داخل الأغشية النفاذة مع طول تلك الأغشية. استطاع هذا النموذج المطور حساب معدل كتلة المياه المحلاه بكفاءة تفوق النموذج التقليدي وبدون الحاجه إلى معاملات ضبط ومعايرة لمعاملات النموذج الرياضي.